Cationic Effects on Photo- and X-ray Radioluminescence of $K_3RE(PO_4)_2$:Ce^{3+}/Pr^{3+} (RE = La, Gd, and Y) Phosphors toward X-ray Detection

Ou, Yiyi; Zhou, Weijie; Dorenbos, Pieter; Liang, Hongbin

Important note
To cite this publication, please use the final published version (if applicable).
Please check the document version above.

Article

Cationic Effects on Photo- and X-ray Radioluminescence of K$_3$RE(PO$_4$)$_2$:Ce^{3+}/Pr^{3+} (RE = La, Gd, and Y) Phosphors toward X-ray Detection

Yiyi Ou, Weijie Zhou, Pieter Dorenbos, and Hongbin Liang*

Read Online

ACCESS | Metrics & More | Article Recommendations | SI Supporting Information

ABSTRACT: Cationic tuning for lanthanide (Ce^{3+}/Pr^{3+})-activated inorganic phosphors with stable, efficient, and fast-decay 5d−4f emissions has emerged as an important strategy toward the continuing pursuit of superior scintillators. The in-depth understanding of the cationic effects on photo- and radioluminescence of lanthanides Ce^{3+} and Pr^{3+} centers is requisite for the rational cationic tuning. Here, we perform a systematic study on the structure and photo- and X-ray radioluminescence properties of K$_3$RE-(PO$_4$)$_2$:Ce^{3+}/Pr^{3+} (RE = La, Gd, and Y) phosphors to elucidate the underlying cationic effects on their 4f−5d luminescence. By using the Rietveld refinements, low-temperature synchrotron−radiation vacuum ultraviolet−ultraviolet spectra, vibronic coupling analyses, and vacuum-referred binding energy schemes, the origins of lattice parameter evolutions, 5d excitation energies, 5d emission energies, and Stokes shifts as well as good emission thermal stabilities of K$_3$RE(PO$_4$)$_2$:Ce^{3+} systems are revealed. In addition, the correlations of Pr^{3+} luminescence to Ce^{3+} in the same sites are also discussed. Finally, the X-ray excited luminescence manifests that the K$_3$Gd(PO$_4$)$_2$:1% Ce^{3+} sample possesses a light yield of ∼10,217 photons/MeV, indicating its potentiality toward X-ray detection application. These results deepen the understanding of cationic effects on Ce^{3+} and Pr^{3+} 4f−5d luminescence and inspire the inorganic scintillator development.
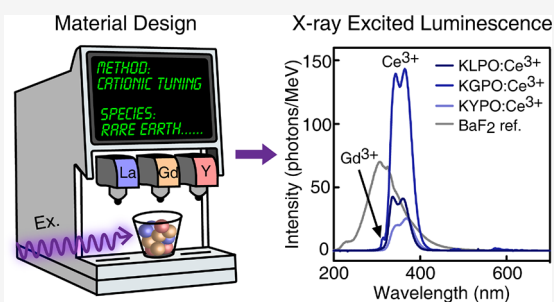
1. INTRODUCTION

Lanthanide (Ce^{3+} and Pr^{3+})-activated inorganic phosphors have attracted tremendous attention in the applications of high-energy radiation detection and medical imaging owing to their stable, efficient, and fast-decay (nanosecond range) 5d−4f emissions.[1−3] For example, the excellent Lu$_{2−x}$Y$_x$SiO$_5$:Ce^{3+} (LYSO:Ce)[4] and Gd$_3$Al$_{5−x}$Ga$_x$O$_{12}$:Ce^{3+} (GAGG:Ce)[5] crystal materials are the commercial scintillators for the positron emission tomography (PET) technique. The LaBr$_3$:Ce^{3+} crystal materials equipped on satellites also play an important role in the cosmic γ-ray detection.[6] With the aim to continuously pursue the superior lanthanide-activated phosphors toward scintillator applications, the composition tuning method has been developed as an essential strategy to modulate the material scintillation properties, such as light yield, decay time, afterglow, and spectral match to photodetectors.[7−9]

In general, the composition tuning for lanthanide (Ce^{3+} and Pr^{3+})-activated phosphors mainly includes the polyhedral unit tuning and cationic tuning. The tuning of polyhedral units such as AlO$_{4/6}$ → GaO$_{4/6}$ or SiO$_4$ → GeO$_4$ evolution usually significantly tailors the electronic band structure of materials, which can inhibit the possible afterglow by removing the shallow traps beneath the conduction band[10] but inevitably affect the 5d−4f luminescence stability of materials.[8,11]

Meanwhile, the tuning of cationic sites (such as Ca^{2+} → Sr^{2+} → Ba^{2+} or Y^{3+} → Gd^{3+} → La^{3+}) for doped Ce^{3+} and Pr^{3+} lanthanides can not only moderately regulate the band gap of materials but also directly modulate their 4f−5d luminescence. The simultaneous modulations for these two aspects are useful to efficiently optimize the scintillation performance of materials.[7,9,12] Fundamentally, the cationic tuning of phosphors tailors the site properties (such as bond length and local vibration) for lanthanide incorporation and further modulates the crystal-field effects, vibronic coupling, and 5d thermal ionization to finally shape the Ce^{3+} and Pr^{3+} 4f−5d luminescence.[13,14] Consequently, the comprehensive knowledge about cationic effects on 4f−5d luminescence is requisite for the rational cationic tuning of phosphors.

In this work, we deliver a systematic study on the structure and photo- and X-ray radioluminescence properties of K$_3$RE(PO$_4$)$_2$:Ce^{3+}/Pr^{3+} (RE = La, Gd, and Y) phosphors to elucidate the cationic effects on 4f−5d luminescence. In fact,
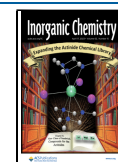
the isomorphic characters among $K_3RE(PO_4)_2$ (RE = La, Gd, and Y) compounds permit their wide cationic tuning.[15] Moreover, when compared to those commercial systems in the garnet structure with high-symmetric sites and the oxyorthosilicate structure with two cationic sites, the Ce^{3+}/Pr^{3+} 4f–5d transitions in $K_3RE(PO_4)_2$ with only one C_s-symmetric RE site manifest well-resolved 5d crystal-field-split excited levels. These features make the $K_3RE(PO_4)_2$ system a suitable platform to reveal the cationic effects on 4f–5d luminescence. Then, by using the Rietveld refinements, low-temperature synchrotron–radiation vacuum ultraviolet–ultraviolet (VUV–UV) spectra, vibronic coupling analyses, and vacuum-referred binding energy schemes, the origins of lattice parameter evolutions, 5d excitation energies, 5d emission energies, and Stokes shifts as well as good emission thermal stabilities of $K_3RE(PO_4)_2:Ce^{3+}$ systems are revealed. The correlations of Pr^{3+} luminescence to Ce^{3+} in the same sites are also studied. Finally, the X-ray excited luminescence of $K_3RE(PO_4)_2:Ce^{3+}/Pr^{3+}$ samples is measured to evaluate the potentiality toward X-ray detection application.

2. EXPERIMENTAL SECTION

2.1. Materials and Synthesis. A series of $K_3RE(PO_4)_2$ (RE = La, Gd, and Y) host compounds and the corresponding $Ce^{3+}/Pr^{3+}/Eu^{3+}$-doped $K_3RE(PO_4)_2$ samples $[K_3RE_{0.99}X_{0.01}(PO_4)_2$, RE = La, Gd, and Y; X = Ce, Pr, and Eu] with a 1% concentration were synthesized with a high-temperature solid-state reaction method. Raw materials including K_2CO_3 (analytical reagent, AR), $NH_4H_2PO_4$ (AR), La_2O_3 (99.99%), Gd_2O_3 (99.99%), Y_2O_3 (99.99%), CeO_2 (99.99%), Pr_6O_{11} (99.99%), and Eu_2O_3 (99.99%) were stoichiometrically weighed and thoroughly mixed in an agate mortar. H_3BO_3 was added as a flux with 5% of total mass of the mixture. Then, the homogeneous mixtures were transferred into corundum crucibles and calcined at 1223 K [for $K_3Y(PO_4)_2$ and $K_3Gd(PO_4)_2$ host/doped samples] or 1423 K [for $K_3La(PO_4)_2$ host/doped samples] for 8 h under CO reducing ambience (for Ce^{3+}/Pr^{3+}-doped samples) or air atmosphere (for Eu^{3+}-doped samples). After cooling down to room temperature (RT) in the furnace, the products were reground into powder for further characterizations.

2.2. Characterizations. Phase purity of samples was checked with a RIGAKU D-MAX 2200 VPC X-ray diffractometer with Cu Kα radiation ($\lambda = 1.5418$ Å) at 40 kV and 26 mA. High-quality X-ray diffraction (XRD) data for Rietveld refinements were collected over a scanning range of 10–110° with an interval of 0.02° on a Bruker D8 Advanced X-ray diffractometer with Cu Kα radiation ($\lambda = 1.5418$ Å) operating at 35 kV and 35 mA. Rietveld refinements were performed with TOPAS Academic Version 4.1 software.[16] VUV–UV excitation and UV–vis emission spectra at 11 K were collected on the 4B8 beamline of Beijing Synchrotron Radiation Facility (BSRF), China. The experimental details can be found elsewhere.[17] The photoluminescence spectra as well as luminescence decay curves in the UV–vis region were measured on an Edinburgh FLS1000 combined spectrometer. A 450 W Xe900 xenon lamp was used as the excitation source for steady-state luminescence measurement; a 290 nm pulsed light-emitting diode (Edinburgh Instruments) was used to measure the luminescence decay curves of Ce^{3+}. The temperature-dependent luminescence measurements at 78–500 K were performed with an Oxford Optistat-DN cryostat, and the sample temperature was controlled by a MercuryiTC temperature controller. The Raman scattering spectra at RT were collected with a Renishaw inVia Qontor Raman microscope upon laser excitation at 532 nm. The X-ray excited luminescence spectra were collected at Delft University of Technology, The Netherlands.[18] A Varian VF-80 J-Pd tube serial number 54719-P6 was used as the X-ray source operated at 80 kV and 1 mA with an 80 W power. The as-prepared samples were pressed into pills, and the BaF_2 crystal was used as a reference. Their emission spectra were measured in the same condition. They were placed at a

distance of about 10 cm from the tube and felt an approximate X-ray flux of 190 Gy/h. The emission was dispersed with an ARC VM504 monochromator (blazed at 300 nm, 1200 grooves mm^{-1}) and measured with a Hamamatsu R943-02 photomultiplier tube (PMT). Due to the well-known scintillation light output of the BaF_2 crystal (~8880 photons/MeV), the light output value of our samples was estimated via the ratio between integrated emission intensities of the sample and BaF_2 under the same measurement conditions.

3. RESULTS AND DISCUSSION

3.1. Crystal Structure and Lattice Parameter Evolution of $K_3RE(PO_4)_2$ (RE = La, Gd, and Y) Compounds and Ce^{3+}/Pr^{3+}-Doped Samples. Isomorphic $K_3RE(PO_4)_2$ (RE = La, Gd, and Y) compounds crystallize in the monoclinic structure with space group $P2_1/m$ (no. 11).[15] Figure 1a shows
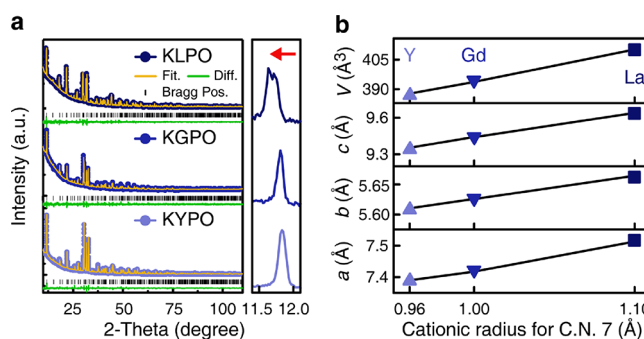

Figure 1. (a) Rietveld refinement results of XRD data of $K_3RE(PO_4)_2$ (RE = La, Gd, and Y) compounds at RT and enlarged patterns in the angle range of 11.4–12.1°. (b) Refined lattice parameters of $K_3RE(PO_4)_2$ compounds.

the collected high-quality XRD data of as-prepared $K_3RE(PO_4)_2$ (RE = La, Gd, and Y) samples (denoted as KLPO, KGPO, and KYPO hereafter, respectively) at RT. They display similar profiles. With the increase in cationic size from Y^{3+} to Gd^{3+} and La^{3+} (Y^{3+}, ~0.96 Å; Gd^{3+}, ~1.00 Å; and La^{3+}, ~1.10 Å for seven coordination surroundings),[19] the XRD peak positions gradually shift to the low-angle direction as illustrated by the enlarged patterns in the right panel, implying the expansion of lattice cells. Rietveld refinement results (Figure 1a and Tables S1–S3) on these XRD data indicate that the synthesized samples possess the pure phase. The extracted lattice parameters (a, b, c, and V) in Figure 1b further validate the lattice cell expansions of compounds with the increasing cationic size. Each parameter (a, b, c, or V) of the La^{3+} compound is the largest, that of the Y^{3+} compound is the smallest, and that of the Gd^{3+} compound is between the two and close to the Y^{3+} compound. This trend is actually consistent with the trend of the radii of the three ions. In the structural framework of these $K_3RE(PO_4)_2$ compounds, there is only one kind of RE^{3+} cationic site. They are similar in geometry and coordinated to seven oxygen ions with C_s symmetry. The average $RE^{3+}-O^{2-}$ bond length values are ~2.34, 2.46, and 2.49 Å for Y^{3+}, Gd^{3+}, and La^{3+} ions, respectively. For Ce^{3+}/Pr^{3+}-doped $K_3RE(PO_4)_2$ samples, Rietveld refinements on their XRD data manifest the pure phase characters (Figures S1 and S2 and Tables S4–S9). Due to the equivalent charge number (+3) and similar effective cationic radii for seven-fold coordination of Ce^{3+} (~1.07 Å), Pr^{3+} (~1.05 Å), Y^{3+}, Gd^{3+}, and La^{3+},[19] the doping Ce^{3+} and Pr^{3+} ions are expected to enter the RE^{3+} sites in $K_3RE(PO_4)_2:Ce^{3+}/Pr^{3+}$ samples.

3.2. Photoluminescence of $K_3RE(PO_4)_2$:Ce^{3+} and Underlying Cationic Effects. 3.2.1. Ce^{3+} VUV–UV Excitation Spectra at 11 K. Figure 2a shows the highest-height
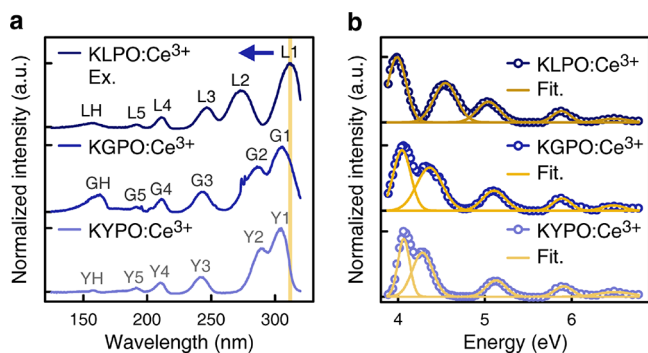
Figure 2. (a) Highest-height normalized VUV−UV excitation (λ_{em} = 335, 340, and 341 nm) spectra of $K_3RE(PO_4)_2$:1%Ce^{3+} (RE = La, Gd, and Y) samples at 11 K, respectively. (b) Fitting results of excitation spectra via a sum of five Gaussian functions.

normalized VUV−UV excitation (λ_{em} = 335, 340, and 341 nm) spectra of $K_3RE(PO_4)_2$:1%Ce^{3+} (RE = La, Gd, and Y) samples at 11 K, respectively. For the KLPO:1%Ce^{3+} sample, the band denoted as LH at ∼157 nm is attributed to the host exciton creation absorption.[20] The corresponding host exciton creation energy (E^{ex}) is ∼7.90 eV. By empirically adding an exciton binding energy [∼0.008 × (E^{ex})^2] to E^{ex},[21] the mobility band gap value (E_g) of the KLPO host is evaluated to be ∼8.39 eV (Table S10). At the long-wavelength side, other five bands (L1−L5) at ∼312, 274, 246, 211, and 191 nm, respectively, pertain to five 5d crystal-field-splitting excited levels ($5d_{1−5}$) of one kind of Ce^{3+} center at the La^{3+} site with low C_s symmetry. Likewise, the host exciton creation absorption bands (marked as GH and YH) are found at ∼163 and 157 nm for KGPO:1%Ce^{3+} and KYPO:1%Ce^{3+} samples, respectively. So, their E_g values are estimated to be ∼8.07 and 8.39 eV (Table S10). The $5d_{1−5}$ excitation bands of Ce^{3+} are observed as ∼305 (G1), 286 (G2), 243 (G3), 211 (G4), and 192 nm (G5) for KGPO:1%Ce^{3+} and ∼304 (Y1), 289 (Y2), 242 (Y3), 210 (Y4), and 191 nm (Y5) for KYPO:1%Ce^{3+}. In addition, the excitation profile of KGPO:1%Ce^{3+} contains some sharp lines at ∼274 and 196 nm due to Gd^{3+} $^8S_{7/2} \rightarrow {}^6I_J$ and $^8S_{7/2} \rightarrow {}^6G_J$ 4f−4f transitions, respectively, implying the possible energy transfer from Gd^{3+} to Ce^{3+} in KGPO. Figure 2b displays the fitting results of excitation spectra in the 3.87−6.78 eV range with a sum of five Gaussian functions to give the estimated energies of Ce^{3+} $5d_{1−5}$ excited levels in $K_3RE(PO_4)_2$:1%Ce^{3+} systems. It provides the energies of Ce^{3+} $5d_{1−5}$ levels as ∼3.99, 4.54, 5.04, 5.88, and 6.49 eV for KLPO:1%Ce^{3+}, ∼4.04, 4.36, 5.10, 5.89, and 6.48 eV for KGPO:1%Ce^{3+}, and ∼4.06, 4.28, 5.13, 5.91, and 6.50 eV for KYPO:1%Ce^{3+}, as listed in Table S10, which show good consistency with the observed peak energies as mentioned above.

From the above data, the Ce^{3+} 5d crystal field splitting values (ε_{cfs}, an energy difference between Ce^{3+} $5d_1$ and $5d_5$ levels) are evaluated as ∼2.50, 2.44, and 2.44 eV in KLPO:1%Ce^{3+}, KGPO:1%Ce^{3+}, and KYPO:1%Ce^{3+}, respectively (Table S10). The Ce^{3+} 5d ε_{cfs} is governed by the shape and size of the first Ce^{3+} coordination polyhedron.[22] The radii of Gd^{3+} and Y^{3+} are very close, so the Ce^{3+} 5d ε_{cfs} values appear the same in KGPO:1%Ce^{3+} and KYPO:1%Ce^{3+}. Herein, it is interesting to further compare the Ce^{3+} 5d ε_{cfs} value in the La^{3+} compound

with that in Gd^{3+}/Y^{3+} compounds. As mentioned in Section 3.1, the lattice parameters of KREPO (RE^{3+} = La^{3+}, Gd^{3+}, and Y^{3+}) decrease according to the relative radius order La^{3+} > Gd^{3+} > Y^{3+}. The change of lattice parameters may be an indication of the size of REO_7 (RE = La, Gd, and Y) coordination polyhedrons. If we think that the shape of the coordination polyhedron is the same in the three cases and only consider the influence of site size, then the 5d ε_{cfs} of Ce^{3+} in the larger La^{3+} site is expected to be smaller than that in smaller Gd^{3+}/Y^{3+} sites, but the experimental observations give just opposite results. It is abnormal that the 5d ε_{cfs} values of Ce^{3+} in KGPO (2.44 eV) and KYPO (2.44 eV) with smaller cationic sites are smaller than that in KLPO (2.50 eV).

This phenomenon implies that in addition to the site size, the site distortion (the change of the first Ce^{3+} coordination polyhedron shape) also has a significant effect on ε_{cfs} values. If only the influence of radius mismatch is considered, then the larger the radius mismatch (ΔR) between the substituted cation and the doping Ce^{3+} ion, the larger the distortion should be. Referring to the radius data of La^{3+} (1.10 Å), Ce^{3+} (1.07 Å), Gd^{3+} (1.00 Å), and Y^{3+} (0.96 Å), it is plausible that the polyhedral shape of CeO_7 is closest to that of LaO_7 and deviates somewhat from GdO_7 while deviates most from YO_7. This means that the shape of the CeO_7 coordination polyhedron is almost the same as that of the LaO_7 polyhedron in KLPO:1%Ce^{3+}, and the shape of the CeO_7 polyhedron may be slightly different from that of the GdO_7 polyhedron in KGPO:1%Ce^{3+}, while the distortion may be somewhat larger when Ce^{3+} ions are incorporated into KYPO. This distortion of the coordination polyhedron may give its additional contribution to the 5d ε_{cfs} values of Ce^{3+} and result in the abnormal smaller 5d ε_{cfs} values of Ce^{3+} in Gd^{3+}/Y^{3+} compounds in comparison to that in the La^{3+} compound.

The careful checking of the experimental 5d energy data in Table S10 also gives support for the different degrees of distortion of the CeO_7 coordination polyhedron in Gd^{3+}/Y^{3+} and La^{3+} compounds since the alteration amplitudes of Ce^{3+} $5d_{1,2,3}$ in the three compounds are different: (i) the $5d_2$ level of Ce^{3+} in KLPO (4.54 eV) gradually goes downward to KGPO (4.36 eV) and KYPO (4.28 eV); (ii) on the contrary, the $5d_3$ level of Ce^{3+} in KLPO (5.04 eV) is lower than those in KGPO (5.10 eV) and KYPO (5.13 eV); however, (iii) the $5d_1$ energy of Ce^{3+} slowly increases according to the relative order in KLPO (3.99 eV), KGPO (4.04 eV), and KYPO (4.06 eV). These observations may be an indication of the different distortions of CeO_7 coordination polyhedrons in the three compounds.

3.2.2. Ce^{3+} UV Emission Spectra at 11 K. Figure 3a displays the highest-height normalized emission (λ_{ex} = 274, 286, and 289 nm) spectra of $K_3RE(PO_4)_2$:1%Ce^{3+} (RE = La, Gd, and Y) samples at 11 K, respectively. They all exhibit the typical doublet emissions originated from the $5d_1 \rightarrow {}^2F_J$ (J = 5/2 and 7/2) transitions of the single Ce^{3+} center. Specifically, the doublet bands are observed at ∼335 (LI, $5d_1 \rightarrow {}^2F_{5/2}$) and 360 nm (LII, $5d_1 \rightarrow {}^2F_{7/2}$) for KLPO:1%$Ce^{3+}$, ∼340 (GI) and 366 nm (GII) for KGPO:1%Ce^{3+}, and ∼341 (YI) and 368 nm (YII) for KYPO:1%Ce^{3+}. These emission bands gradually shift to longer wavelength from KLPO to KGPO and KYPO systems. Figure 3b presents the Gaussian fitting results of emission spectra with a sum of two functions. It provides the detailed Ce^{3+} $5d_1 \rightarrow {}^2F_J$ (J = 5/2 and 7/2) doublet emission energies of ∼3.68 and 3.43 eV for KLPO:1%Ce^{3+}, ∼3.65 and 3.38 eV for KGPO:1%Ce^{3+}, and ∼3.64 and 3.37 eV for
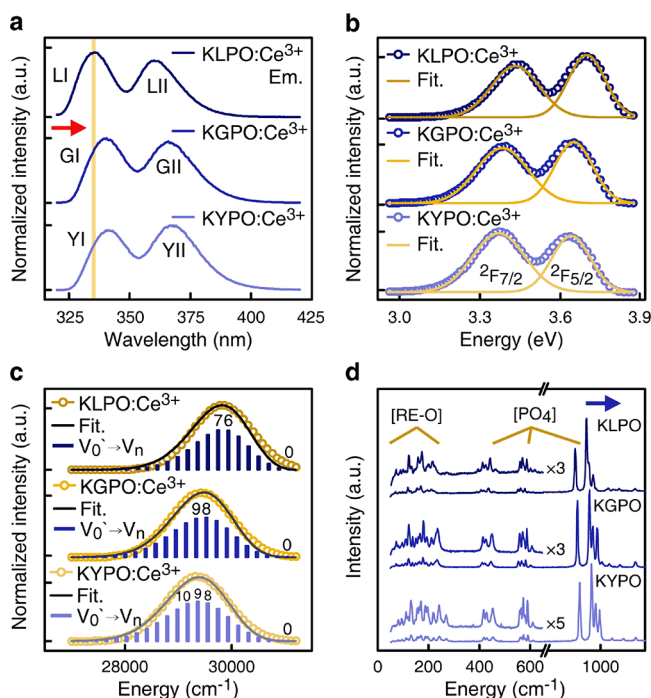
Figure 3. (a) Highest-height normalized emission (λ_{ex} = 274, 286, and 289 nm) spectra of $K_3RE(PO_4)_2$:1%Ce^{3+} (RE = La, Gd, and Y) samples at 11 K, respectively. (b) Fitting results of emission spectra via a sum of two Gaussian functions. (c) Vibronic coupling analysis on the Ce^{3+} $5d_1 \rightarrow {}^2F_{5/2}$ emission band. (d) Raman scattering spectra of $K_3RE(PO_4)_2$ (RE = La, Gd, and Y) samples at RT and the enlarged curves in the range of 50−650 cm^{-1}.

KYPO:1%Ce^{3+}. The energy differences between the above doublet bands fall in the range of 0.25−0.27 eV, which is close to the common value (0.25 eV) for the single Ce^{3+} case. Furthermore, the corresponding Stokes shift (ΔE_S) values turn larger as ~0.31 (~2.50×10^3), 0.39 (3.15×10^3), and 0.42 eV (3.39×10^3 cm^{-1}) from KLPO to KGPO and to KYPO systems, respectively (Table S11). To study the spectroscopic origin of increasing ΔE_S values and red-shifted Ce^{3+} emission, the vibronic coupling analysis on the Ce^{3+} $5d_1 \rightarrow {}^2F_{5/2}$ emission profile extracted from Figure 3b was conducted based on the single-configurational coordination model.[13,14] Under the assumption that both the Ce^{3+} 4f−5d excitation and emission electronic transitions couple to the same effective vibration mode, the ΔE_S and full-width of half maximum (FWHM, Γ) values of Ce^{3+} $5d_1 \rightarrow {}^2F_{5/2}$ emission can be described with the Huang−Rhys factor (S) and effective phonon energy ($\hbar\omega$) as follows:

$$\Delta E_S = (2S - 1)\hbar\omega \tag{1}$$

$$\Gamma(T) = \sqrt{8\ln 2}\,\hbar\omega\left[S\cdot\coth\left(\frac{\hbar\omega}{2kT}\right)\right]^{1/2} \tag{2}$$

where T is the temperature in Kelvin and k is the Boltzmann constant (6.950×10^{-1} cm^{-1}/K). With the experimental values of ΔE_S and Γ values in Table S11, the S and $\hbar\omega$ values are calculated as ~7.08 and 189.9 cm^{-1} for KLPO:1%Ce^{3+}, ~8.77 and 190.1 cm^{-1} for KGPO:1%Ce^{3+}, and ~9.40 and 190.3 cm^{-1} for KYPO:1%Ce^{3+}. To further verify these obtained vibronic coupling factors, the corresponding Ce^{3+} $5d_1 \rightarrow {}^2F_{5/2}$ emission curves were simulated via a simplified spectral function (eq 3) with these two factors:[13]

$$I = \frac{e^{-S}S^p}{p!}\left(1 + S^2\frac{e^{-\hbar\omega/kT}}{p + 1}\right), \quad p = \frac{E_0 - E}{\hbar\omega} \tag{3}$$

where p is the effective phonon number and E_0 is the zero-phonon line (ZPL) energy. Figure 3c presents the good consistency between the experimental lines and simulated profiles. In addition, the estimated E_0 values are ~31,050, 31,050, and 31,080 cm^{-1} for KLPO, KGPO, and KYPO systems, respectively (Table S11), which are close to the intersection points (~30,930, 30,940, and 31,060 cm^{-1}) between the corresponding excitation and emission profiles for each system (Figure S3). These successful simulation results indicate that the obtained vibronic coupling factors (S and $\hbar\omega$) could suitably describe the vibronic coupling processes in $K_3RE(PO_4)_2$:1%Ce^{3+} samples despite the simplicity of the single-configurational coordination model. Based on these two factors, the discrete phonon lines with the Poisson intensity distributions ($e^{-S} \cdot S^p/p!$) are depicted in Figure 3c. They exhibit similar envelopes with the experimental curves. The numbers of participant phonons when the phonon line intensity reaches maximum are ~7, 8, and 9 for KLPO, KGPO, and KYPO systems, respectively, which are near the obtained S values (Table S11) and approximately reflect the gradually larger vibronic coupling degrees. Moreover, the evaluated effective phonon energies ($\hbar\omega$), viz., the energy intervals between discrete phonon lines, are located in the low wavenumber vibrational signal range (<250 cm^{-1}) of the Raman scattering spectra of $K_3RE(PO_4)_2$ compounds (Figure 3d). These low-wavenumber vibrational signals are mainly contributed to the $[REO_7]$-related local vibrations and lattice translation.[23] Due to the synergistic effects of cationic RE^{3+} atomic mass and RE^{3+}−O^{2-} bond length,[24] these $[REO_7]$-related vibrations along with the $[PO_4]$-related vibrations (bending modes @ 400−600 cm^{-1}; stretching modes @ 900−1100 cm^{-1}) gradually blue-shift to the higher wavenumber side from KLPO to KYPO systems (Figure 3d). Therefore, we deem that the stronger vibronic coupling of Ce^{3+} 4f−5d electronic transitions to the $[REO_7]$-related vibrations with incremental effective phonon energies from KLPO to KYPO systems lead to their larger ΔE_S value and red-shifted Ce^{3+} emissions.

3.2.3. Ce^{3+} Temperature-Dependent Emissions from 78 to 500 K. To investigate the Ce^{3+} emission thermal stabilities of samples, the temperature-dependent (78−500 K) emission (λ_{ex} = 274, 286, and 289 nm) spectra and luminescence decay curves of $K_3RE(PO_4)_2$:1%Ce^{3+} (RE = La, Gd, and Y), respectively, were collected (Figures S4 and S5). Figure 4a presents the calculated Ce^{3+} emission lifetimes from the decay curves with single-exponential properties (Figure S5). At the same temperature, the three curves are very close to each other, indicating that the small variation of emission wavelength has no significant effect on the fluorescence lifetime. With the rise of temperature, they show the slight increase tendency, and the increase magnitude seems to follow the relative order KLPO:1%Ce^{3+} > KGPO:1%Ce^{3+} > KYPO:1% Ce^{3+}. These nearly stable lifetimes indicate that the Ce^{3+} emissions of all the samples do not experience the thermal quenching in the temperature range of 78−500 K and possess good thermal stabilities. The slight increase in lifetimes might be due to the reabsorption of Ce^{3+} emission driven by the overlapping between excitation and emission spectra because the relative order of increasing lifetime in Figure 4a is just the relative order of the decreasing Stokes shift in Table S11.[25]
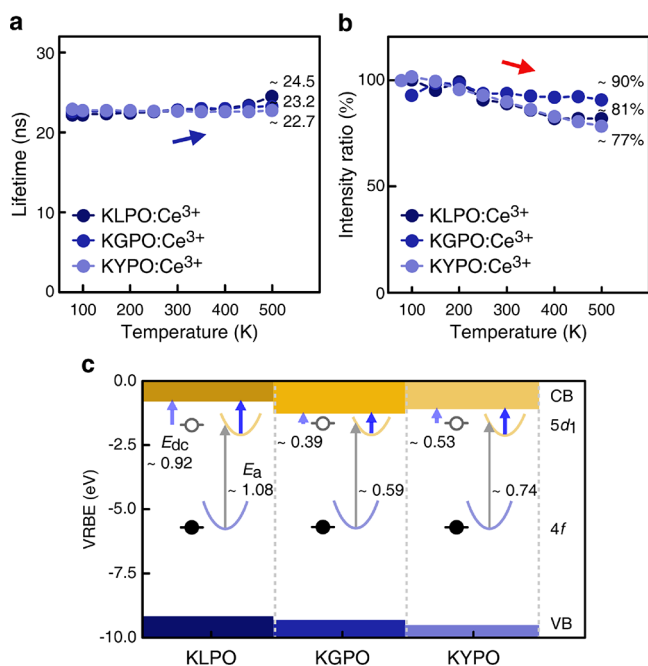
Figure 4. (a) Temperature-dependent (78−500 K) lifetime values of Ce^{3+} emissions of $K_3RE(PO_4)_2$:1%Ce^{3+} (RE = La, Gd, and Y) samples. (b) Temperature-dependent (78−500 K) integrated emission (λ_{ex} = 274, 286, and 289 nm) intensity ratios of $K_3RE(PO_4)_2$:1%Ce^{3+} (RE = La, Gd, and Y) samples, respectively. (c) VRBE schemes of Ce^{3+} $5d_1$ excited states, 4f ground states, and host compound band structures of $K_3RE(PO_4)_2$:1%Ce^{3+} (RE = La, Gd, and Y) samples.

Accordingly, the most spectral overlapping of the KLPO:1% Ce^{3+} sample originated from its smallest ΔE_S value ($\sim$2.50 × 10^3 cm^{-1}) leads to the relative clear increase in lifetime (Figure S6).

As for the temperature-dependent Ce^{3+} emission intensity of samples, the extracted integrated Ce^{3+} emission intensity ratios of the elevated temperatures to 78 K in Figure 4b gradually decrease. The integrated emission intensities at 500 K turn $\sim$81, 90, and 77% of intensity at 78 K for KLPO, KGPO, and KYPO systems, respectively. This trend is somewhat different from the above-mentioned temperature-dependent lifetime tendency since the emission intensity could be affected by various factors including temperature dependence of absorption strength and reabsorption.[25]

In fact, due to the proximity of the Ce^{3+} $5d_1$ emitting level to the host compound conduction band (CB) bottom, the 5d electron thermal ionization to host compound CB is regarded as an important thermal quenching mechanism for Ce^{3+} emission in the dilute doping case.[26,27] To study the 5d thermal ionization mechanism for good thermal stability of $K_3RE(PO_4)_2$:1%Ce^{3+} samples, the vacuum-referred binding energy (VRBE) schemes of lanthanides in $K_3RE(PO_4)_2$ hosts were constructed to probe the correlations between the Ce^{3+} 5d state and CB bottom.[28−30] The necessary parameters and procedures for VRBE construction are compiled in Table S13 in the Supporting Information. Figure 4c and Table S13 tabulate the obtained VRBEs of Ce^{3+} $5d_1$ excited states, 4f ground states, valence band (VB) top, and CB bottom of $K_3RE(PO_4)_2$ compounds. The VRBE E_{VB} value of VB top that is dominated by the O 2p orbital gradually decreases from KLPO (approximately −9.20 eV) to KGPO (−9.33 eV) and to

KYPO (−9.51 eV), which indicates their stronger binding trends relative to the vacuum level and is consistent with the shorter RE^{3+}−O^{2-} bonds.[31] Meanwhile, the E_{CB} of CB bottom that is dominated by the RE d and f orbitals decreases from KLPO (approximately −0.81 eV) to KGPO (−1.27 eV) and then increases for the KYPO (−1.11 eV) case. The similar E_{CB} distributions were also reported in RE_2BaZnO_5[32] and $REPO_4$[33] compounds. As for the $E(4f)$ of the Ce^{3+} well-shield 4f ground state, it remains quite stable ranging from −5.72 to −5.70 eV among $K_3RE(PO_4)_2$ systems. The $E(5d_1)$ for the Ce^{3+} lowest 5d excited state gradually increases from KLPO to KYPO cases. Hence, the energy gap (E_{dc}) values between the E_{CB} and Ce^{3+} $E(5d_1)$ can be observed as $\sim$0.92, 0.39, and 0.53 eV for KLPO, KGPO, and KYPO cases, respectively. When further considering the vibronic coupling lowering in the Ce^{3+} $5d_1$ excited states (see the $5d_1$ excited parabola in Figure 4c), the corresponding possible thermal-quenching activation energies (E_a) in the framework of the 5d thermal-ionization mechanism are $\sim$1.08, 0.59, and 0.74 eV by adding the half of Stokes shift values.[34−36] These relatively large values imply that the inactive 5d thermal-ionization process would be the main reason for good thermal stability of Ce^{3+} emissions in $K_3RE(PO_4)_2$ systems.

3.3. Photoluminescence of $K_3RE(PO_4)_2$:Pr^{3+} and Correlations to Ce^{3+} Luminescence. Figure 5a presents the highest-height normalized VUV−UV excitation spectra of $K_3RE(PO_4)_2$:1%Pr^{3+} (RE = La, Gd, and Y) samples at 11 K by monitoring different emission wavelengths. For KLPO:1%Pr^{3+}, the two excitation curves upon 248 and 267 nm emissions overlap to each other. This indicates that there is only one kind of Pr^{3+} luminescent center and accords with the result of
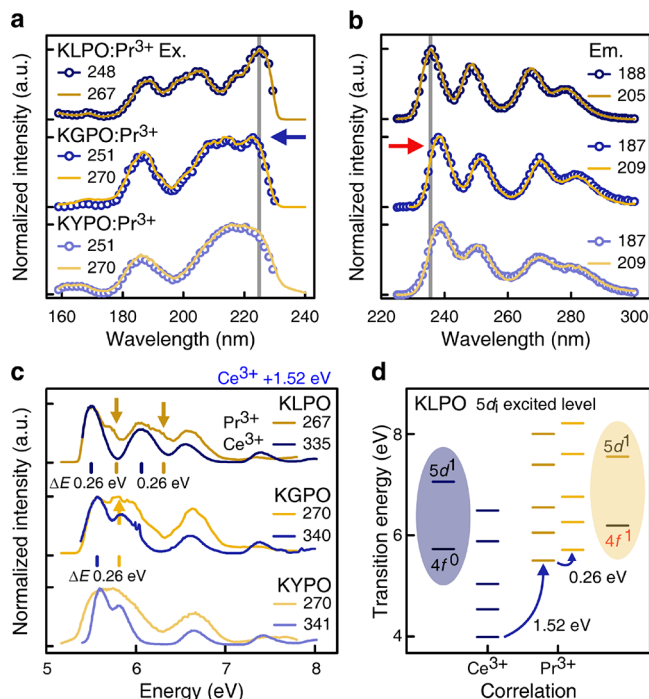
Figure 5. (a) Highest-height normalized VUV−UV excitation and (b) emission spectra of $K_3RE(PO_4)_2$:1%Pr^{3+} (RE = La, Gd, and Y) samples at 11 K by monitoring different wavelengths. (c) Comparison between Pr^{3+} excitation and Ce^{3+} excitation (after shifting 1.52 eV to high-energy direction) profiles in $K_3RE(PO_4)_2$ compounds. (d) Correlations of $5d_i$ excited levels of Pr^{3+} to those of Ce^{3+}.

KLPO:1%Ce^{3+}. The broad excitation bands in the 160−240 nm range are ascribed to the transitions from 4f ground states to 5d excited states ($4f^1[^2F_J]5d_i$) of Pr^{3+}.[37] When it turns to KGPO and KYPO systems, they also keep the similar spectral profiles by monitoring different wavelengths. Notably, the lowest 5d excitation band of Pr^{3+} gradually shifts to a shorter wavelength and the 5d excitation bands become broader and more structureless from KLPO to KGPO and KYPO. These phenomena are possibly due to the smaller crystal field splitting of Pr^{3+} across KLPO-KGPO-KYPO series, which are analogue to Ce^{3+} results as discussed above.

The emission spectra of $K_3RE(PO_4)_2$:1%Pr^{3+} (RE = La, Gd, and Y) samples at 11 K in Figure 5b exhibit the similar profiles under different excitation wavelengths. They all contain four evident emission bands in the wavelength range of 220−300 nm, which are originated from the transitions from the relaxed lowest Pr^{3+} 5d excited state ($4f^1[^2F_{5/2}]5d_1$) to the 4f ground states ($^3H_{4,5,6}$ and $^3F_{2,3,4}$).[38] Similar to the Ce^{3+} emissions in Figure 3a, the positions of Pr^{3+} emissions gradually shift to the longer wavelength side across KLPO-KGPO-KYPO series, which result from the increased Stokes shift driven by stronger vibronic coupling.

To further correlate the 5d excitations of Pr^{3+} with Ce^{3+}, Figure 5c shows the comparison of the excitation profiles of Ce^{3+} after a 1.52 eV high-energy-shift and Pr^{3+} in $K_3RE(PO_4)_2$ compounds. They show good consistency in the peak positions of the first three 5d excited levels in the 5−7 eV range, especially for KLPO and KGPO cases. Despite the band broadening in the KYPO system, their excitation energies of Pr^{3+} and Ce^{3+} $5d_{1-3}$ levels are approximately matched. As for the Pr^{3+} higher excitation bands above 7 eV, they seem weaker and more inconspicuous than the shifted Ce^{3+} bands, which may be due to their proximity to the host conduction band bottom. Therefore, it can be deemed that the crystal field effects on the 5d excited level distributions are almost the same for the Ce^{3+} and Pr^{3+} cases. The dominant spectroscopic structure of Pr^{3+} excitation bands could be reproduced by shifting the Ce^{3+} bands to the higher energy side by an energy of 1.52 eV. This energy originates from the energy difference between the first 5d excited levels of free Ce^{3+} (49,340 cm^{-1}) and Pr^{3+} (61,580 cm^{-1}) ions,[39] which is mainly contributed by their electron binding energy difference of 4f ground states relative to vacuum.

The estimated Pr^{3+} $5d_i$ excited levels in the KLPO compound as the representative are depicted in Figure 5d. Moreover, different from the Ce^{3+} case with only one 4f electron, the remaining $4f^1$ core of Pr^{3+} $4f^1[^2F_J]5d_i$ excited states would further impose its perturbation effect on the 5d excited levels and engender the corresponding satellite bands at the higher energy sides of $5d_i$ excitation bands. Owing to the narrow-band feature and suitable energy difference of excitation bands in the KLPO:Pr^{3+} case, the satellite bands of $5d_{1-2}$ excited levels could be partially resolved in Figure 5c. The corresponding splitting energies are ~0.26 eV, which is slightly larger than the splitting energies (~0.25 eV) of Ce^{3+} spin−orbital-coupled $^2F_{5/2}$ and $^2F_{7/2}$ 4f ground states, as discussed in Figure 3b. The similar result could be also observed in the KGPO:Pr^{3+} case. Figure 5d finally illustrates the correlation between Ce^{3+} and Pr^{3+} 5d excited levels in the KLPO case with two high-energy-shifted energies of 1.52 and 0.26 eV.

3.4. X-ray Excited Luminescence of $K_3RE(PO_4)_2$:Ce^{3+}/ Pr^{3+} at RT. Figure 6 displays the emission spectra of
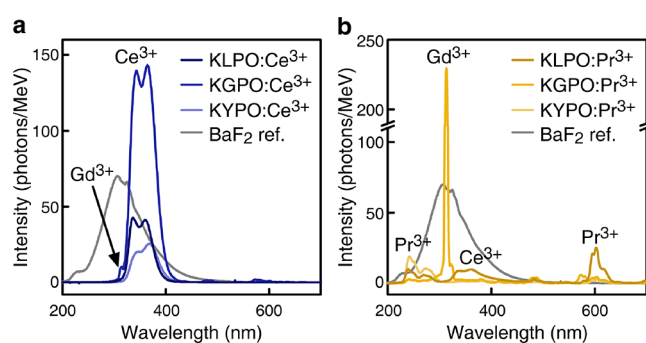
Figure 6. X-ray excited luminescence spectra of (a) $K_3RE(PO_4)_2$:1% Ce^{3+} and (b) $K_3RE(PO_4)_2$:1%Pr^{3+} (RE = La, Gd, and Y) samples at RT.

$K_3RE(PO_4)_2$:1%Ce^{3+} and $K_3RE(PO_4)_2$:1%Pr^{3+} (RE = La, Gd, and Y) samples under X-ray excitation at RT. For Ce^{3+}-activated samples, they all exhibit the typical Ce^{3+} doublet emissions with the same wavelengths as the photoluminescence in Figure 3a. The KGPO:1%Ce^{3+} sample shows the highest Ce^{3+} emissions among three samples with the same Ce^{3+} concentration (1%). In addition, the weak Gd^{3+} emission at ~313 nm also appears in this sample. The clear deviation from the exponential decay of Gd^{3+} luminescence ($\lambda_{ex} = 274$ nm, $\lambda_{em} = 311$ nm) of KGPO:1%Ce^{3+} in Figure S7 directly evidences the occurrence of the energy transfer (ET) from Gd^{3+} to Ce^{3+} ions in this system.[40] The efficient ET process sensitizes the Ce^{3+} luminescence under X-ray excitation while largely degrades the Gd^{3+} emission. For Pr^{3+}-activated samples, they show the weak Pr^{3+} f−d emissions in the 200−300 wavelength range. Especially, the KGPO:1%Pr^{3+} sample manifests weak Pr^{3+} f−d emission with strong Gd^{3+} emission. This hints that the ET from Pr^{3+} f−d transitions to Gd^{3+} would take effect. The appearance of Pr^{3+} f−d excitations in the excitation spectrum of the KGPO:1%Pr^{3+} sample when monitoring the Gd^{3+} emission at 312 nm (Figure S8) confirms this thought. Therefore, the different scintillation light yields of Ce^{3+} and Pr^{3+} in KGPO are mainly due to their different roles in the ET process. Except for the Pr^{3+} f−d emissions, the KLPO:1%Pr^{3+} sample also displays the relatively intense f−f emissions of Pr^{3+} at 603 nm, which are ascribed to the $^1D_2 \rightarrow {}^3H_J$ transitions. The extra 4f−4f depopulation pathways of Pr^{3+} are also a possible reason for the low light output. The underlying mechanism of the fluorescence branch between Pr^{3+} f−d and f−f emissions under X-ray excitation is important for the design of Pr^{3+}-activated ultrafast scintillators, which we would pursue in the following work. Additionally, the Ce^{3+} emission in the 300−400 wavelength range in the KLPO:1% Pr^{3+} sample is due to the presence of Ce^{3+}-related impurities.

Finally, to evaluate the light yields of samples under X-ray excitation, the X-ray excited luminescence of BaF_2 crystal reference with a known light yield of ~8800 photons/MeV is also collected under the same conditions in Figure 6. By comparing the integrated emission intensities of our samples and BaF_2 reference, the light yield results of $K_3RE(PO_4)_2$:1% Ce^{3+} and $K_3RE(PO_4)_2$:1%Pr^{3+} (RE = La, Gd, and Y) samples are tabulated in Table 1. The KGPO:1%Ce^{3+} sample possesses the highest light yield of ~10,217 photons/MeV among samples. This light yield result is close to those (~11,100 and 14,100 photons/MeV) of $NaGd(PO_3)_4$:1%Ce^{3+} and $KGd(PO_3)_4$:1%Ce^{3+} materials,[41] respectively, which indicates that

Table 1. Estimated Light Yield Results of $K_3RE(PO_4)_2$:1% Ce^{3+} and $K_3RE(PO_4)_2$:1%Pr^{3+} (RE = La, Gd, and Y) Samples at RT

light yield (photons/MeV)	$K_3RE(PO_4)_2$:1%Ce^{3+}	$K_3RE(PO_4)_2$:1%Pr^{3+}
La	2793	2576
Gd	10,217	3186
Y	1777	1237

the KGPO:1%Ce^{3+} material could be served as a potential candidate for X-ray detection application.

4. CONCLUSIONS

In summary, we have revealed the structural properties and cationic effects on the luminescence of $K_3RE(PO_4)_2$:Ce^{3+}/Pr^{3+} (RE = La, Gd, and Y) phosphors in depth and demonstrated the $K_3Gd(PO_4)_2$:1%Ce^{3+} sample with a light yield of ~10,217 photons/MeV and fast decay (~23 ns) as a potential candidate toward X-ray detection application. Via the Rietveld refinements, we found that the synthesized samples exhibit the pure phase and the doped lanthanides are incorporated in the cationic RE^{3+} sites. The VUV−UV excitation spectra at 11 K manifest the detailed Ce^{3+} 5d excited levels of K_3RE-$(PO_4)_2$:Ce^{3+} samples. Anomalously, the crystal field splitting (ε_{cfs}) of Ce^{3+} 5d excited levels in the La^{3+} site with a larger size displays a larger value (~2.50 eV) than that (~2.44 eV) of smaller Y^{3+}/Gd^{3+} sites. This results from the possible site distortions in Y^{3+} and Gd^{3+} cases driven by the size mismatch between doping ions and cationic sites. The vibronic coupling analyses show that across La-Gd-Y series, the gradually stronger vibronic coupling between Ce^{3+} 4f−5d transitions and $K_3RE(PO_4)_2$ compounds with larger RE-related vibrational energies causes the KLPO:1%Ce^{3+} emissions with the smallest Stokes shift (~2.50 × 10^3 cm^{-1}) and highest energies (~3.68 and 3.43 eV). Notably, the Ce^{3+} emissions of $K_3RE(PO_4)_2$:Ce^{3+} samples all possess the good thermal stability, which are verified by the large energy gap values (0.39−0.92 eV) between Ce^{3+} $5d_1$ levels and RE orbital-rich host conduction band bottoms in the view of the VRBE scheme. In addition, the Pr^{3+} 5d excited levels are understood with a blue-shifting of ~1.52 eV for the difference between the $5d_1$ levels of free Pr^{3+} and Ce^{3+} and further with a blue-shifting of ~0.26 eV for the perturbation effect of the Pr^{3+} remaining $4f^1$ core on 5d excited levels. Finally, owing to the efficient ET from Gd^{3+} to Ce^{3+}, the $K_3Gd(PO_4)_2$:1%Ce^{3+} material exhibits the highest light yield of ~10,217 photons/MeV among samples. This work can be served as a paradigm for the in-depth analysis on Ce^{3+}/Pr^{3+}-activated inorganic phosphors and inspire the novel inorganic scintillator exploration.

ASSOCIATED CONTENT

Ⓢ Supporting Information

The Supporting Information is available free of charge at https://pubs.acs.org/doi/10.1021/acs.inorgchem.3c00566.

> Rietveld refinement results, temperature-dependent excitation, emission spectra and decay curves of $K_3RE(PO_4)_2$:1%Ce^{3+}, low-temperature VUV−UV spectra of $K_3RE(PO_4)_2$:1%Eu^{3+} and KGPO:1%Pr^{3+}, and VRBE scheme construction process of $K_3RE(PO_4)_2$ (PDF)

AUTHOR INFORMATION

Corresponding Author

Hongbin Liang − *MOE Key Laboratory of Bioinorganic and Synthetic Chemistry, KLGHEI of Environment and Energy Chemistry, School of Chemistry, Sun Yat-sen University, Guangzhou 510006, China;* ⊙ orcid.org/0000-0002-3972-2049; Email: cesbin@mail.sysu.edu.cn

Authors

Yiyi Ou − *MOE Key Laboratory of Bioinorganic and Synthetic Chemistry, KLGHEI of Environment and Energy Chemistry, School of Chemistry, Sun Yat-sen University, Guangzhou 510006, China;* ⊙ orcid.org/0000-0002-2111-5064

Weijie Zhou − *MOE Key Laboratory of Bioinorganic and Synthetic Chemistry, KLGHEI of Environment and Energy Chemistry, School of Chemistry, Sun Yat-sen University, Guangzhou 510006, China;* ⊙ orcid.org/0000-0001-5199-9836

Pieter Dorenbos − *Department of Radiation Science and Technology, Faculty of Applied Sciences, Delft University of Technology, 2629 JB Delft, The Netherlands*

Complete contact information is available at:
https://pubs.acs.org/10.1021/acs.inorgchem.3c00566

Author Contributions

Conceptualization: Y.O. and H.L.; data curation and formal analysis: Y.O., W.Z., and H.L.; funding acquisition: H.L.; investigation and methodology: Y.O. and W.Z.; project administration, resources, and supervision: H.L.; validation: Y.O. and H.L.; visualization: Y.O. and W.Z.; writing-original draft: Y.O.; writing-review and editing: Y.O., W.Z., P.D., and H.L.

Notes

The authors declare no competing financial interest.

ACKNOWLEDGMENTS

REFERENCES

(1) Qin, X.; Liu, X.; Huang, W.; Bettinelli, M.; Liu, X. Lanthanide-Activated Phosphors Based on 4f-5d Optical transitions: Theoretical and Experimental Aspects. *Chem. Rev.* **2017**, *117*, 4488−4527.

(2) Nikl, M.; Yoshikawa, A. Recent R&D Trends in Inorganic Single-Crystal Scintillator Materials for Radiation Detection. *Adv. Opt. Mater.* **2015**, *3*, 463−481.

(3) Huang, M.; Li, Q.-L.; Yuan, R.; Yang, X.-C.; Yin, G.-Z.; Yang, X.-X.; Hu, J.-F.; Gao, X.-Y.; Deng, Z.; Wang, L.; Zhao, J.-T.; Zhang, Z.-J. Improved Phase Stability and Enhanced Luminescence of Calcite Phase $LuBO_3$:Ce^{3+} through Ga^{3+} Incorporation. *Inorg. Chem.* **2020**, *59*, 14513−14525.

(4) Cooke, D. W.; McClellan, K. J.; Bennett, B. L.; Roper, J. M.; Whittaker, M. T.; Muenchausen, R. E.; Sze, R. C. Crystal Growth and Optical Characterization of Cerium-Doped $Lu_{1.8}Y_{0.2}SiO_5$. *J. Appl. Phys.* **2000**, *88*, 7360−7362.

(5) Kamada, K.; Endo, T.; Tsutumi, K.; Yanagida, T.; Fujimoto, Y.; Fukabori, A.; Yoshikawa, A.; Pejchal, J.; Nikl, M. Composition Engineering in Cerium-Doped $(Lu,Gd)_3(Ga,Al)_5O_{12}$ Single-Crystal Scintillators. *Cryst. Growth Des.* **2011**, *11*, 4484−4490.

(6) van Loef, E. V. D.; Dorenbos, P.; van Eijk, C. W. E.; Krämer, K. W.; Güdel, H. U. Scintillation Properties of LaBr$_3$:Ce^{3+} Crystals: Fast, Efficient and High-Energy-Resolution Scintillators. *Nucl. Instrum. Methods Phys. Res., Sect. A* **2002**, *486*, 254−258.

(7) Jary, V.; Nikl, M.; Kurosawa, S.; Shoji, Y.; Mihokova, E.; Beitlerova, A.; Pazzi, G. P.; Yoshikawa, A. Luminescence Characteristics of the Ce^{3+}-Doped Pyrosilicates: The Case of La-Admixed Gd$_2$Si$_2$O$_7$ Single Crystals. *J. Phys. Chem. C* **2014**, *118*, 26521−26529.

(8) Vrubel, I. I.; Polozkov, R. G.; Shelykh, I. A.; Khanin, V. M.; Rodnyi, P. A.; Ronda, C. R. Bandgap Engineering in Yttrium-Aluminum Garnet with Ga Doping. *Cryst. Growth Des.* **2017**, *17*, 1863−1869.

(9) Lin, L.; Shi, R.; Zhou, R.; Peng, Q.; Liu, C.; Tao, Y.; Huang, Y.; Dorenbos, P.; Liang, H. The Effect of Sr^{2+} on Luminescence of Ce^{3+}-Doped (Ca,Sr)$_2$Al$_2$SiO$_7$. *Inorg. Chem.* **2017**, *56*, 12476−12484.

(10) Fasoli, M.; Vedda, A.; Nikl, M.; Jiang, C.; Uberuaga, B. P.; Andersson, D. A.; McClellan, K. J.; Stanek, C. R. Band-Gap Engineering for Removing Shallow Traps in Rare-Earth Lu$_3$Al$_5$O$_{12}$ Garnet Scintillators Using Ga^{3+} Doping. *Phys. Rev. B* **2011**, *84*, No. 081102.

(11) Ogiegło, J. M.; Katelnikovas, A.; Zych, A.; Jüstel, T.; Meijerink, A.; Ronda, C. R. Luminescence and Luminescence Quenching in Gd$_3$(Ga,Al)$_5$O$_{12}$ Scintillators Doped with Ce^{3+}. *J. Phys. Chem. A* **2013**, *117*, 2479−2484.

(12) Lin, L.; Ning, L.; Zhou, R.; Jiang, C.; Peng, M.; Huang, Y.; Chen, J.; Huang, Y.; Tao, Y.; Liang, H. Site Occupation of Eu^{2+} in Ba$_{2−x}$Sr$_x$SiO$_4$ (x = 0−1.9) and Origin of Improved Luminescence Thermal Stability in the Intermediate Composition. *Inorg. Chem.* **2018**, *57*, 7090−7096.

(13) Henderson, B.; Imbusch, G. F. *Optical Spectroscopy of Inorganic Solids*; Oxford University Press, 2006.

(14) Brik, M. G.; Ma, C.-G. *Theoretical spectroscopy of transition metal and rare earth ions: from free state to crystal field*; Jenny Stanford Publishing, 2020.

(15) Farmer, J. M.; Boatner, L. A.; Chakoumakos, B. C.; Rawn, C. J.; Richardson, J. Structural and crystal chemical properties of alkali rare-earth double phosphates. *J. Alloys Compd.* **2016**, *655*, 253−265.

(16) Coelho, A. A. *TOPAS. Academic*; Ver 4.1; Coelho Software: Brisbane, Australia, 2007.

(17) Tao, Y.; Huang, Y.; Gao, Z.; Zhuang, H.; Zhou, A.; Tan, Y.; Li, D.; Sun, S. Developing VUV spectroscopy for protein folding and material luminescence on Beamline 4B8 at the Beijing Synchrotron Radiation Facility. *J. Synchrotron Radiat.* **2009**, *16*, 857−863.

(18) Yang, Y.; Lou, B.; Ou, Y.; Su, F.; Ma, C.-G.; Duan, C.-K.; Dorenbos, P.; Liang, H. Experimental and Theoretical Studies of the Site Occupancy and Luminescence of Ce^{3+} in LiSr$_4$(BO$_3$)$_3$ for Potential X-ray Detecting Applications. *Inorg. Chem.* **2022**, *61*, 7654−7662.

(19) Shannon, R. D. Revised Effective Ionic Radii and Systematic Studies of Interatomic Distances in Halides and Chalcogenides. *Acta Crystallogr., Sect. A: Cryst. Phys., Diffr., Theor. Gen. Crystallogr.* **1976**, *A32*, 751−767.

(20) Schwarz, L.; Finke, B.; Kloss, M.; Rohmann, A.; Sasum, U.; Haberland, D. Investigations on the electronic structure of double phosphates of the type M$_3$RE(PO$_4$)$_2$ (RE = rare earths, lanthanides). *J. Lumin.* **1997**, *72-74*, 257−259.

(21) Dorenbos, P. Charge transfer bands in optical materials and related defect level location. *Opt. Mater.* **2017**, *69*, 8−22.

(22) Dorenbos, P. 5d-Level Energies of Ce^{3+} and the Crystalline Environment. III. Oxides Containing Ionic Complexes. *Phys. Rev. B* **2001**, *64*, 125117.

(23) Matraszek, A.; Godlewska, P.; Macalik, L.; Hermanowicz, K.; Hanuza, J.; Szczygieł, I. Optical and thermal characterization of microcrystalline Na$_3$RE(PO$_4$)$_2$:Yb orthophosphates synthesized by Pechini method (RE = Y, La, Gd). *J. Alloys Compd.* **2015**, *619*, 275−283.

(24) Nakamoto, K. *Infrared and Raman Spectra of Inorganic and Coordination Compounds, part A: Theory and Applications in Inorganic Chemistry*; John Wiley & Sons, 2009.

(25) Bachmann, V.; Ronda, C.; Meijerink, A. Temperature Quenching of Yellow Ce^{3+} Luminescence in YAG:Ce. *Chem. Mater.* **2009**, *21*, 2077−2084.

(26) Dorenbos, P. Thermal Quenching of Eu^{2+} 5d-4f Luminescence in Inorganic Compounds. *J. Phys.: Condens. Matter* **2005**, *17*, 8103−8111.

(27) Ueda, J.; Dorenbos, P.; Bos, A. J. J.; Meijerink, A.; Tanabe, S. Insight into the Thermal Quenching Mechanism for Y$_3$Al$_5$O$_{12}$:Ce^{3+} through Thermoluminescence Excitation Spectroscopy. *J. Phys. Chem. C* **2015**, *119*, 25003−25008.

(28) Dorenbos, P. Modeling the Chemical Shift of Lanthanide 4f Electron Binding Energies. *Phys. Rev. B* **2012**, *85*, 165107.

(29) Dorenbos, P. The Nephelauxetic Effect on the Electron Binding Energy in the 4f^1 Ground State of Lanthanides in Compounds. *J. Lumin.* **2019**, *214*, 116536.

(30) Dorenbos, P. Improved Parameters for the Lanthanide 4f^1 and 4f^{q-1}5d Curves in HRBE and VRBE Schemes that Takes the Nephelauxetic Effect into Account. *J. Lumin.* **2020**, *222*, 117164.

(31) Luo, H.; Bos, A. J. J.; Dorenbos, P. Charge Carrier Trapping Processes in RE$_2$O$_2$S (RE = La, Gd, Y, and Lu). *J. Phys. Chem. C* **2017**, *121*, 8760−8769.

(32) Srivastava, A. M.; Camardello, S. J.; Dorenbos, P.; Brik, M. G. Vacuum Referred Binding Energy Scheme for Rare Earth Ions in RE$_2$BaZnO$_5$ [RE = Y, La, Gd]. *Opt. Mater.* **2017**, *70*, 57−62.

(33) Lyu, T.; Dorenbos, P. Charge Carrier Trapping Processes in Lanthanide Doped LaPO$_4$, GdPO$_4$, YPO$_4$, and LuPO$_4$. *J. Mater. Chem. C* **2018**, *6*, 369−379.

(34) Poncé, S.; Jia, Y.; Giantomassi, M.; Mikami, M.; Gonze, X. Understanding Thermal Quenching of Photoluminescence in Oxynitride Phosphors from First Principles. *J. Phys. Chem. C* **2016**, *120*, 4040−4047.

(35) Zhou, W.; Ou, Y.; Huang, L.; Song, E.; Ma, F.; Xia, Z.; Liang, H.; Zhang, Q. Shining Transparent Displays with Stable Narrow-Band Blue-Emitting Phosphor in Layered Film. *Adv. Mater.* **2022**, 2206278.

(36) Dorenbos, P. Thermal quenching of lanthanide luminescence via charge transfer states in inorganic materials. *J. Mater. Chem. C* **2023**, DOI: 10.1039/D2TC04439K.

(37) Dorenbos, P. Exchange and Crystal Field Effects on the 4f^{n-1}5d levels of Tb^{3+}. *J. Phys.: Condens. Matter* **2003**, *15*, 6249−6268.

(38) Ueda, J.; Meijerink, A.; Dorenbos, P.; Bos, A. J. J.; Tanabe, S. Thermal ionization and thermally activated crossover quenching processes for 5d-4f luminescence in Y$_3$Al$_{5-x}$Ga$_x$O$_{12}$:Pr^{3+}. *Phys. Rev. B* **2017**, *95*, No. 014303.

(39) Dorenbos, P. The 4f^n → 4f^{n-1}5d Transitions of the Trivalent Lanthanides in Halogenides and Chalcogenides. *J. Lumin.* **2000**, *91*, 91−106.

(40) Ou, Y.; Zhou, W.; Ma, F.; Liu, C.; Zhou, R.; Su, F.; Huang, Y.; Dorenbos, P.; Liang, H. Luminescence Tuning of Ce^{3+}, Pr^{3+} Activated (Y,Gd)AGG System by Band Gap Engineering and Energy Transfer. *J. Rare Earths* **2020**, *38*, 514−522.

(41) Zhong, J.; Liang, H.; Su, Q.; Zhou, J.; Khodyuk, I. V.; Dorenbos, P. Radioluminescence Properties of Ce^{3+}-Activated MGd(PO$_3$)$_4$ (M = Li, Na, K, Cs). *Opt. Mater.* **2009**, *32*, 378−381.